communications biology

A Nature Portfolio journal

Article

https://doi.org/10.1038/s42003-025-08175-9

SEC24D depletion induces osteogenic differentiation deficiency by inactivating the ATF6/TGF-β/Runx2 regulatory loop

Jing Zhang[1,6], Kai Yang[2,6], Wen-qi Chen[1,6], Dong-lan Sun[1], Hua-ying Hu[3], Qian Li[4], You-sheng Yan[2], Ya-zhou Li[5], Cheng-hong Yin[2] ✉ & Qing Guo[1] ✉

Protein coat complexes strongly influence intracellular cargo trafficking. Coatopathies represent a wide range of genetic conditions caused by mutations in protein coat components. The *SEC24D* gene, which encodes a Sec24 isoform that constitutes a cargo-specific capturer in the COPII coat, is responsible for a rare type of autosomal recessive osteogenesis imperfecta. We report an OI patient. Clinical and imaging findings suggested that the patient had OI. Genetic detection by whole-exome sequencing (WES) identified a compound heterozygous *SEC24D* variants, including c.2609_2610delGA (p. R870fs*10) and c.938G>A (p. R313H). In silico analysis suggested that the missense R313H mutation most likely affects protein stability and secondary structure. In vitro studies showed that knockdown or mutation of *SEC24D* affected the osteogenic differentiation of mesenchymal stem cells (MSCs) and inducted ER stress. Transcriptomic sequencing suggested that the TGF-β pathway mediated the destructive effect of SEC24D depletion on osteogenic differentiation. Further experiments confirmed that ATF6 participated in regulating the TGF-β pathway and osteogenic biomarkers by SEC24D. This study identified a *SEC24D* variation causing OI, which expanded the mutation spectrum of this gene. Further studies on the mechanism of action showed that SEC24D defects may induce osteogenic differentiation deficiency by inactivating the ATF6/TGF-β/Runx2 regulatory loop.

Eukaryotic proteostasis is maintained by a network of pathways that control protein synthesis, folding, trafficking, aggregation, disaggregation, and degradation[1]. In the secretory pathway, protein coat complexes are the major components responsible for the delivery of different types of proteins or lipids to specific locations in the cell[2]. They were initially proposed to be organized into (a) a membrane-proximal inner or adaptor layer and (b) a membrane-distal, outer, or scaffold layer, which sequentially assemble from cytosolic components on the target membranes. They assemble on the cytosolic face of membranes to promote cargo sorting and the formation of transport carriers in the endomembrane system of eukaryotic cells[2,3]. The known protein coats include COPI, COPII, AP-1, AP-2, AP-3, AP-4, AP-5, and retromer[4].

Coatopathies are a group of genetic disorders caused by defects in various components of protein coats and impairment of normal intracellular vesicular trafficking[4]. Nearly 30 different coatopathies affecting different tissues and organs in humans have been identified[4]. The COPII complex is a two-layered coat associated with ER-exit sites (ERESs), which mediate protein export from the ER toward the ER-Golgi intermediate compartment (ERGIC) and cis-Golgi cisternae[5]. It comprises an inner layer of SEC23-SEC24 dimers and an outer layer of SEC132-SEC312 heterotetramers, sequentially recruited to form a flexible cage around vesicles[6,7]. Clarified diseases caused by mutations in COPII components include cranio-lenticulo-sutural dysplasia (CLSD; Boyadjiev-Jabs syndrome; MIM #607812; by *SEC23A* mutation), congenital dyserythropoietic anemia type

---

[1]Prenatal Diagnosis Center, Shijiazhuang Obstetrics and Gynecology Hospital; Hebei Key Laboratory of Maternal and Fetal Medicine; Shijiazhuang Key Laboratory of Reproductive Health, Shijiazhuang, Hebei, China. [2]Prenatal Diagnosis Center, Beijing Obstetrics and Gynecology Hospital, Capital Medical University, Beijing, China. [3]Medical Innovation Research Division of Chinese, PLA General Hospital, Beijing, China; Jiaen Genetics Laboratory, Beijing Jiaen Hospital, Beijing, China. [4]Prenatal Diagnosis Center, Department of Obstetrics and Gynaecology, Sixth Medical Center, Chinese PLA General Hospital, Beijing, China. [5]Department of Pediatric Orthopedic, The Third Hospital of Hebei Medical University, Shijiazhuang, Hebei, China. [6]These authors contributed equally: Jing Zhang, Kai Yang, Wen-qi Chen. ✉e-mail: yinchh@ccmu.edu.cn; yfguoqing@163.com

II (CDAII; MIM #224100; by *SEC23B* mutation), and Cole-Carpenter syndrome 2 (CLCRP2; MIM #616294; by *SEC24D* mutation)[8–10].

The *SEC24D* gene, located at chromosomal region 4q26 and spanning 115.8 kb of gDNA, encodes one of the four isoforms of Sec24, which is responsible for identifying and capturing different cargos in COPII[11]. Garbes et al. initially established the pathogenic relationship between *SEC24D* mutations and a severe syndromic type of osteogenesis imperfecta (OI)[10]. Four studies also reported this association, but the patients in these studies exhibited a vast range of symptom severity and phenotypic variability[12–15]. The genotype-phenotype association is poorly understood due to the lack of a large number of case cohorts and variations.

In this study, one patient with moderate OI was assessed and underwent clinical and genetic investigations. Moreover, an immunohistochemistry (IHC) examination was performed on paraffin sections of the patient's tissue. A compound heterozygous variation in *SEC24D* was identified. Subsequently, in silico protein structural analysis was conducted to predict the specific intramolecular effect of a missense variant on this variation. In vitro experiments, including translational sequencing and molecular biological validation, were also conducted to determine the effect of SEC24D defects on the function and form of osteoblasts.

Results

Clinical, imaging, H&E, and IHC manifestations of the patient

After being diagnosed with OI, the patient underwent multiple surgeries to manage fractures in 2014, 2015, and 2020. The X-ray results before and after surgery in 2020 are shown in Fig. 1. After the pathological fracture of both femurs, the left femur was curved, the density of the fracture end was uneven, the surrounding callus was formed, and internal fixation was present (Fig. 1H–L). Additionally, the bones in the patient's skull and trunk were poorly developed, and her dentition was irregular (Fig. 1C, E–G).

To determine the effect of the *SEC24D* mutation on osteogenic differentiation. We collected femoral tissues from the patient. First, H&E staining revealed fibrous tissue proliferation accompanied by bleeding between trabeculae, femur lamellar bone tissue, and abnormal mineralization of bone trabeculae (Fig. 1M–O). Next, femoral tissues were collected from patients and normal control,s and the expression of RUNX2 and OCN in these samples was detected. The protein levels of RUNX2 and OCN were significantly lower in affected tissues than in normal tissues (Fig. 1P–S). These results indicated that osteogenic differentiation was inhibited.

Genetic findings

The results of the CMA revealed no clinically significant copy number variations (CNVs). WES revealed a compound heterozygous variation in the *SEC24D* gene, consisting of two variants, i.e., c.938G>A (p. R313H) and c.2609_2610delGA (p. R870fs*10), which were inherited from the parents (Fig. 2A). The c.2609_2610delGA (p. R870fs*10) variant was reported for the first time. The location of both variants at the level of the nucleic acid and peptide chains of this gene are shown in Fig. 2B. These two variants affected two amino acid residues at their respective locations, causing them to change, and the results of the MEGA7 analysis showed that the two residues maintained cross-species conservation, which supported the pathogenicity of the two variants (Fig. 2C).

To further understand the effect of the missense variant of p.R313H on the structure of the SEC24D protein, we conducted a series of in silico analyses. Briefly, the SEC24D R313H variant affects protein stability and secondary structure by altering the number of hydrogen bonds, decreasing the compactness, and increasing the exposed surface area of the protein (Supplementary Material 1).

SEC24D defects affect the function and form of human osteoblasts by inactivating the ATF6/TGF-β/Runx2 regulatory loop in vitro

Knockdown or mutation of SEC24D affects osteogenic differentiation of mesenchymal stem cells. First, we constructed sh SEC24D-NC, sh SEC24D-1, sh SEC24D-2, and sh SEC24D-3 expression vectors. Only the effective knockdown sequence was packaged into adenoviruses for use in subsequent experiments. After the hBMSCs were transfected for 48 h, we detected the level of expression of *SEC24D* mRNA. The results showed significant downregulation of *SEC24D* mRNA expression in the shSEC24D-1, shSEC24D-2, and shSEC24D-3 groups compared to the control group and shSEC24D-NC group ($P < 0.05$), confirming that the knockdown plasmid was constructed (Fig. 3A). The viability of the transfected cells was examined using a CCK-8 assay. The knockdown of *SEC24D* significantly decreased the viability of cells compared to the viability of the cells transfected with shSEC24D NC (Fig. 3B). Moreover, the mutation of *SEC24D* significantly decreased the viability of cells compared to that of cells expressing SEC24D WT. As ALP plays a key role in osteogenic differentiation, subsequent detection of ALP levels in shSEC24D-NC-, shSEC24D-, SEC24D-WT-, and SEC24D-MUT-transfected cells was performed using ELISA and staining methods. ELISA was used to detect the ALP content in the transfected cells on days 1, 7, and 14, revealing a significant decrease in the ALP level in the shSEC24D group compared to that in the shSEC24D-NC group on days 1, 7, and 14 ($P < 0.05$). Additionally, compared to SEC24D-WT, SEC24D-MUT showed a significant decrease in ALP levels on days 7 and 14 ($P < 0.05$) (Fig. 3C). ALP staining yielded consistent results (Fig. 3D and E). The findings were validated by Alizarin Red staining. Staining of sh SEC24D-NC-, sh SEC24D-, SEC24D-WT-, and SEC24D-MUT-transfected cells revealed a significant decrease in the Alizarin Red content in the sh SEC24D group compared to that in the sh SEC24D-NC group ($P < 0.05$). Moreover, compared to SEC24D-WT, SEC24D-MUT significantly decreased the Alizarin Red content ($P < 0.05$) (Fig. 3F and G). Western blotting analysis was performed to detect the level of expression of ALP, RUNX2, OPN, and OCN proteins in different transfected cell groups. Compared to those in the sh SEC24D-NC group, the expression levels of ALP, RUNX2, OPN, and OCN proteins in the sh SEC24D group were significantly lower ($P < 0.05$). Similarly, compared to SEC24D-WT, SEC24D-MUT significantly decreased the level of expression of ALP, RUNX2, OPN, and OCN proteins ($P < 0.05$) (Fig. 3H and I). Western blotting analysis of the expression of the Bglap, Colla1, Osteonectin, and Osteris proteins in different groups of transfected cells revealed a significant decrease in the shSEC24D group compared to that in the shSEC24D-NC group ($P < 0.05$). Additionally, SEC24D-MUT significantly decreased Bglap, Colla1, Osteonectin, and Osteris protein expression compared to SEC24D-WT ($P < 0.05$) (Fig. 3J and K).

SEC24D mutation downregulates RUNX2 and collagen I and promotes ER stress. To assess the transport of collagen and osteogenic proteins in stem cells, immunofluorescence staining was performed using protein disulfide isomerase (PDI)/Colla1 and PDI/RUNX2 in different transfection groups. The staining results revealed that the level of expression of Colla1 and RUNX2 proteins in the sh SEC24D group was significantly lower than that in the sh SEC24D-NC group ($P < 0.05$). In the SEC24D-MUT group, the protein expression levels of Colla1 and RUNX2 were significantly lower than those in the SEC24D-WT group ($P < 0.05$) (Fig. 4A, B). These results suggested that SEC24D is a key factor in the synthesis and transport of collagen and osteogenic proteins in stem cells. To elucidate the regulatory mechanism of SEC24D in osteogenesis, transmission TEM was performed to observe the endoplasmic reticulum (ER) in the different transfection groups. In the TEM images, the rough ER in the shSEC24D-NC group exhibited a track-like dense and coherent arrangement, with ribosomes attached to the ER surface. In contrast, the ER in the sh-SEC24D group exhibited swelling, fragmentation, and disrupted coherence, with ribosome detachment. The ER status in the SEC24D-MUT group was also lower than that in the SEC24D-WT group. These results indicated that the *SEC24D* mutation can promote ER stress (Fig. 4C).

SEC24D regulates osteogenesis by modulating the expression of RUNX2 and ATF6-N. The ATF6 gene, located at 1q23.3 and consisting of

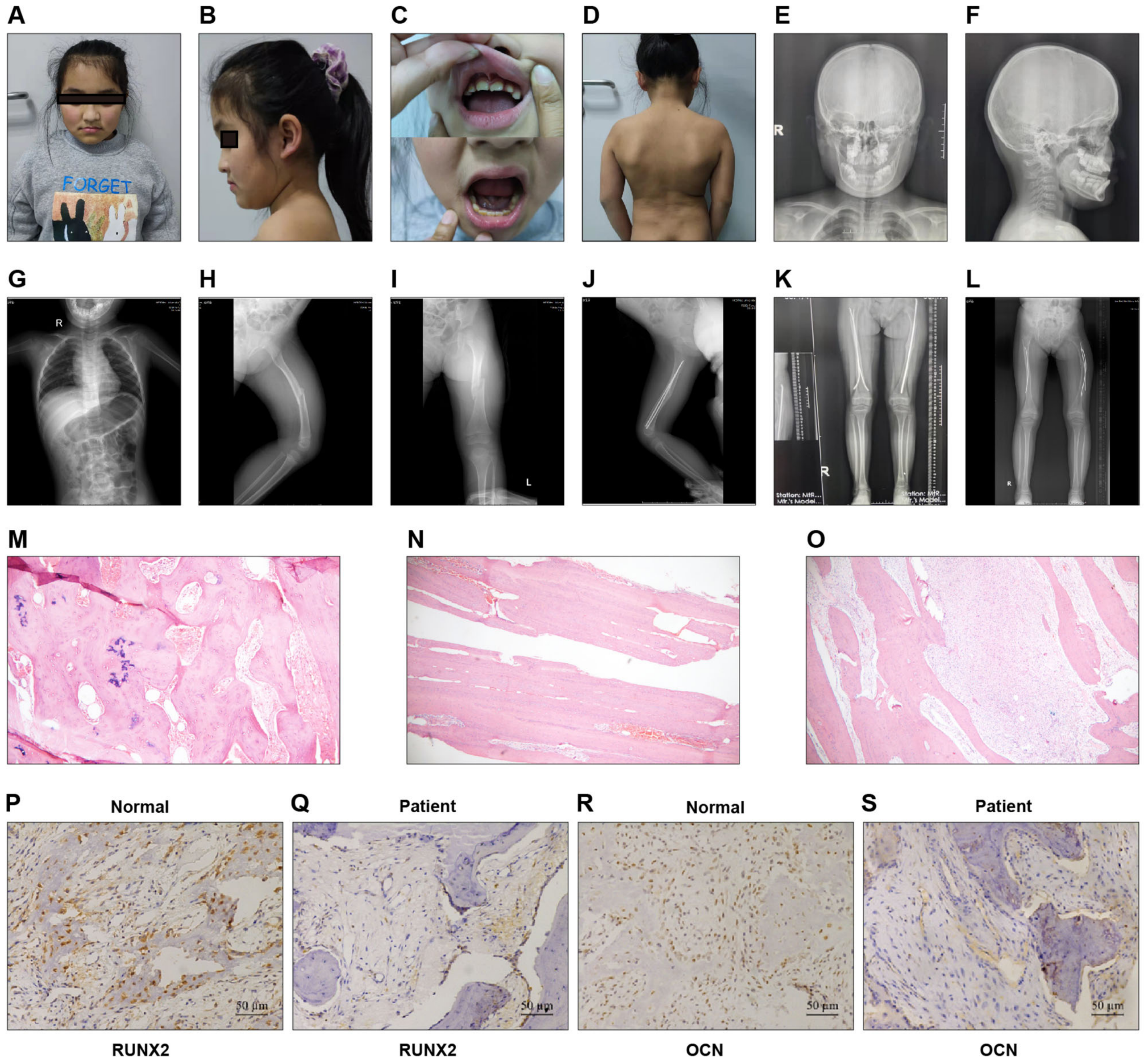

Fig. 1 | The examination of patients included in this study. A–D Photos of the patient's face, teeth, and back. **E–L** X-ray examination of the patient. **M–O** HE examination of femoral tissues. **P**-**S**. Immunohistochemistry detection of RUNX2 and OCN protein expression levels in femoral tissues of patients and normal people.

17 exons, is the main regulatory factor of ER stress response genes[16]. ATF6 is sequentially hydrolyzed by the proteases S1P and S2P in the Golgi apparatus, releasing the soluble transcription factor ATF6-N. ATF6-N translocates to the nucleus and binds to the ER stress response element (ERS) in the unfolded protein response (UPR) gene promoter, producing downstream effects that alleviate ER stress[17]. When ER stress persists, it can lead to diseases such as chondrodysplasia and osteoarthritis[18,19]. To determine the regulatory mechanism of SEC24D in osteogenesis, an ATF6 overexpression plasmid was constructed. The sh SEC24D-NC group, sh SEC24D group, and OE-ATF6/sh SEC24D co-transfection group were used for the experiments. ALP staining was performed on cells from the sh SEC24D-NC, sh SEC24D, and OE-ATF6/sh SEC24D transfection groups. Compared to that in the sh SEC24D-NC group, the ALP content in the sh SEC24D group was significantly lower ($P < 0.05$), while the ALP content in the OE-ATF6/sh SEC24D group was significantly greater than that in the sh SEC24D group ($P < 0.05$) (Fig. 5A). Subsequently, the results were further validated using Alizarin Red staining. Staining of cells from the SEC24D-NC group, shSEC24D group, and OE-ATF6/sh SEC24D co-transfection group revealed a significant decrease in the Alizarin Red content in the shSEC24D group compared to that in the shSEC24D-NC group ($P < 0.05$). The Alizarin Red content was significantly higher in the OE-ATF6/sh SEC24D group compared to that in the sh SEC24D group ($P < 0.05$) (Fig. 5B). The results of the qPCR analysis revealed that OE-ATF6 did not regulate *SEC24D* mRNA expression but upregulated RUNX2 expression in cells (Fig. 5C). Similar results were obtained at the protein level (Fig. 5D and E). Immunofluorescence staining of OPN/RUNX2 revealed that the shSEC24D group had significantly lower levels of RUNX2 protein expression than the shSEC24D-NC group ($P < 0.05$). The expression of RUNX2 protein was significantly higher in the OE-ATF6/sh SEC24D group compared to that in the sh SEC24D group ($P < 0.05$) (Fig. 5F).

Transcriptomic sequencing revealed the involvement of TGF-β signaling pathway on osteogenic differentiation by SEC24D knockdown. To determine the molecular mechanisms and signaling pathways of SEC24D in the osteogenic differentiation of human mesenchymal stem cells, transcriptome sequencing was conducted. Using Venn diagrams and heat maps, sequencing data analysis revealed

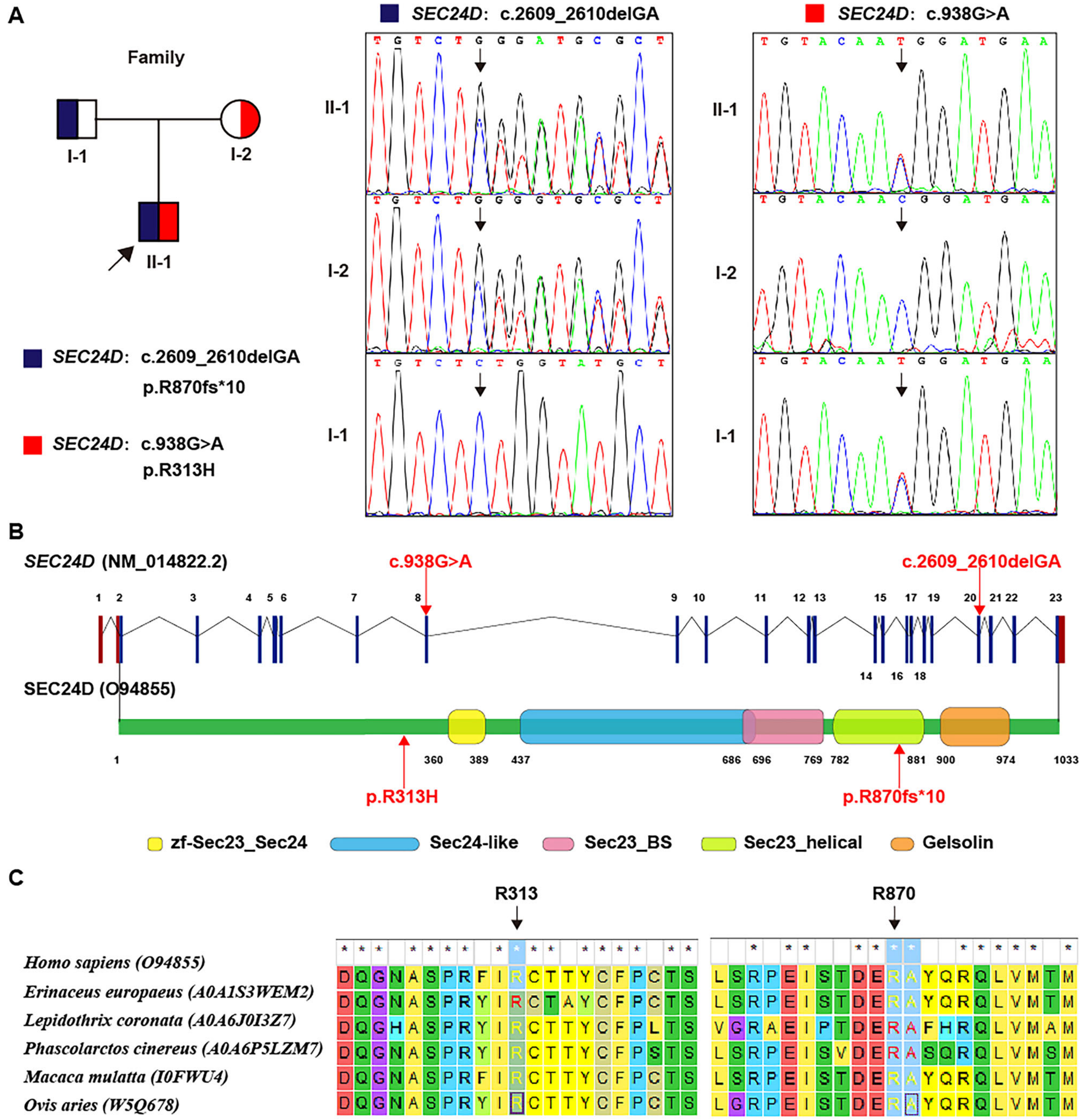

Fig. 2 | Genetic analysis of the patient's causative variation. **A** A compound heterozygous variation in the SEC24D gene was identified. **B** The location at the nucleic acid and peptide chain levels of the SEC24D gene. **C** The cross-species conservation of the two residues identified by MEGA7 analysis.

that compared to the NC group, the *SEC24D* knockdown group exhibited 371 upregulated gene sets and 350 downregulated gene sets (Fig. 6A and B). KEGG analysis of the DEGs revealed a close relationship between SEC24D regulation and the TGF-β signaling pathway (Fig. 6C). To confirm the bioinformatics prediction results, sh-ATF6-NC and sh-ATF6 cell transfections were performed. The qPCR analysis was conducted to detect the level of expression of ATF6-N, TGF-β, and RUNX2. Compared to the sh-ATF6-NC group, the sh-ATF6 group showed a significant reduction in the level of expression of TGF-β and RUNX2, which indicated that sh-ATF6 influences the expression of TGF-β and RUNX2 (Fig. 6D–F). The results of the WB analysis confirmed these findings (Fig. 6G–J). Then, ATF6 was analyzed, RUNX2 and TGF-β1 initiation binding sites were detected, and luciferase reporter assays were conducted to verify the binding of ATF6 to RUNX2 and TGF-β1. The results showed that ATF6 lost its original regulatory function after the binding sites of RUNX2 and TGF-β1 were mutated (Fig. 6K and L). Finally, the results of ChIP analysis revealed that among the three binding sites, ATF6 exhibited the highest binding affinity for RUNX2 and TGF-β1 at site 1 (Fig. 6M and N). These results demonstrated that ATF6-N regulates transcription of Runx2 and TGF-β1. Bone tissues were collected from patients and normal controls, and the expression of ATF6 and TGF-β in these samples was detected. The protein levels of ATF6 and TGF-β were lower in affected tissues than in normal tissues (Fig. 6O–R). These results indicated that ATF6 and TGF-β were associated with OI in vivo.

ATF6-N and TGF-β pathway concertedly regulate the transcription of RUNX2. To elucidate the mechanism by which the TGF-β signaling pathway regulates SEC24D, we treated cells with the KRFK TFA. The

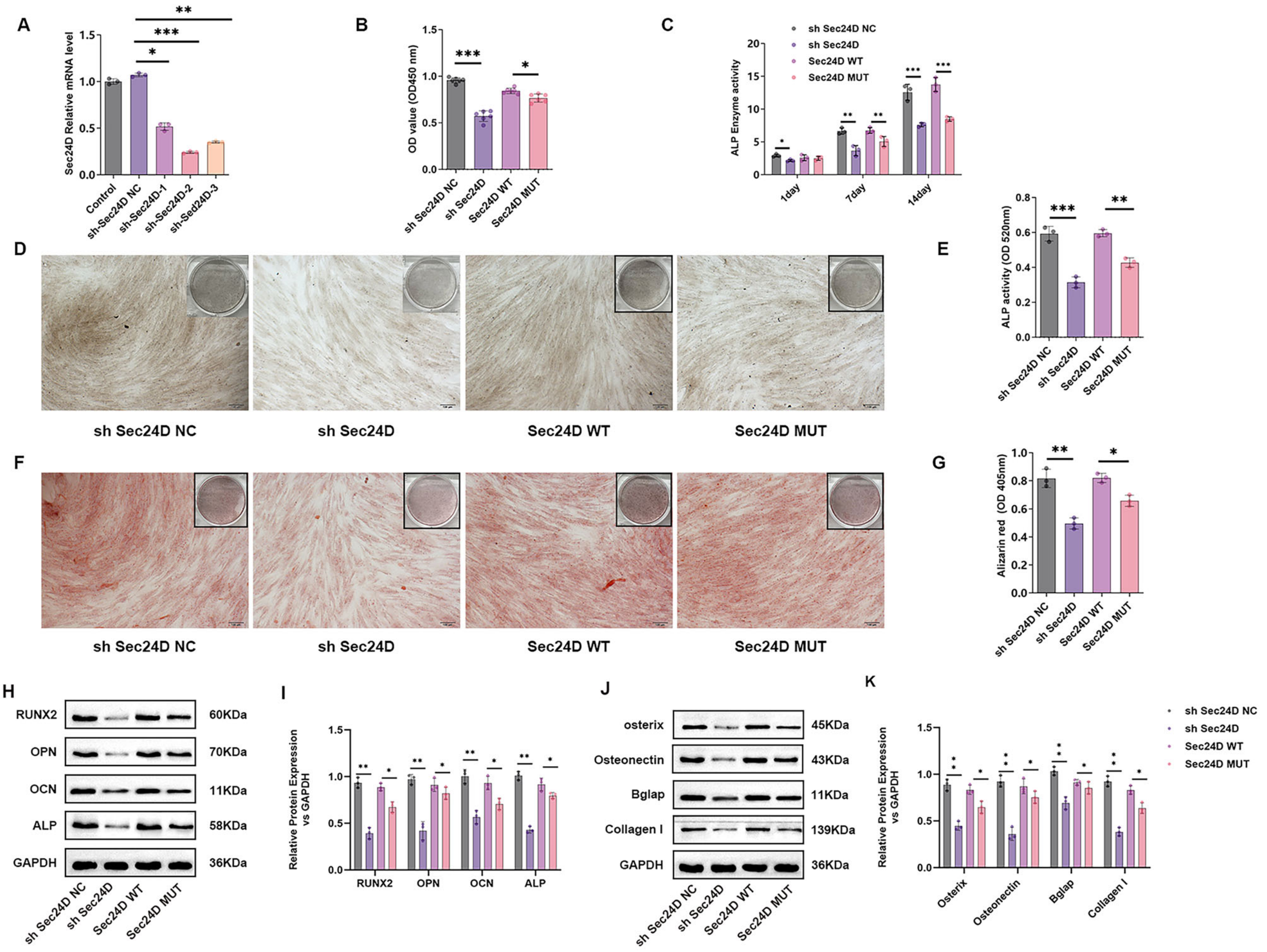

Fig. 3 | Knockdown or mutation of SEC24D affects the osteogenic differentiation of mesenchymal stem cells. A Expression validation of different transfected groups. **B** The viability of different transfected groups. **C** ELISA detection of ALP in different transfected groups. **D** ALP staining in different transfected groups. **E** Statistical analysis of ALP staining in different transfected groups. **F** Alizarin Red staining in different transfected groups. **G** Statistical analysis of Alizarin Red staining in different transfected groups. **H** Western blot detection of ALP, RUNX2, OPN, and OCN protein expression levels in different transfected groups. I Statistical analysis of ALP, RUNX2, OPN, and OCN protein expression. **J** Western blot analysis of Bglap, Colla1, Osteonectin, and Osteris protein expression in different transfected groups. **K** Statistical analysis of Bglap, Colla1, Osteonectin, and Osteris protein expression. $n = 3$ independent experiments. The error bars are equivalent throughout the Figure.

cells were divided into sh-ATF6-NC, sh-ATF6, and sh-ATF6/KRFK TFA groups for intervention. ALP staining was performed on cells from different groups. The ALP content in the sh-ATF6 group was significantly lower than that in the sh-ATF6-NC group ($P < 0.05$), while it was significantly higher in the sh-ATF6/KRFK TFA group compared to that in the sh-ATF6 group ($P < 0.05$) (Fig. 7A). These results were confirmed using Alizarin Red staining. The cells from the sh-ATF6-NC, sh-ATF6, and sh-ATF6/KRFK TFA groups were stained, revealing a significant decrease in the Alizarin Red content in the sh-ATF6 group compared to that in the sh-ATF6-NC group ($P < 0.05$). The sh-ATF6/KRFK TFA group showed a significant increase in Alizarin Red content compared to the sh-ATF6 group ($P < 0.05$) (Fig. 7B). The qPCR and WB assays revealed that KRFK TFA effectively regulated the expression of S1P, S2P, ATF6, SEC24D, and RUNX2 at the protein and transcription levels (Fig. 7C, D). Finally, immunofluorescence staining of different transfection groups was performed using Ghost Peptide/RUNX2. The staining results showed that the sh-ATF6 group exhibited significantly lower levels of the RUNX2 protein than the sh-ATF6-NC group ($P < 0.05$), while the sh-ATF6/KRFK TFA group showed significantly higher levels of RUNX2 protein than the sh-ATF6 group (Fig. 7E) ($P < 0.05$).

TGF-β regulates the expression of S1P and S2P. Plasmids overexpressing S1P and S2P, designated OE S1P and OE S2P, respectively, were constructed. Cells were independently transfected with sh-TGF-β, and four treatment groups were established: sh-TGF-βNC, sh-TGF-β, sh-TGF-β + OE S1P, and sh-TGF-β + OE S2P. ALP and Safranin O staining was performed on cells from different groups. Compared to the sh-TGF-β-NC group, the sh-TGF-β group exhibited a significant decrease in the ALP and Safranin O content ($P < 0.05$). The sh-TGF-β + OE S1P and sh-TGF-β + OE S2P groups showed a significant increase in ALP and Safranin O content than the sh-TGF-β group ($P < 0.05$) (Fig. 8A, B). The results of the qPCR and WB analyses revealed significant regulation of the transcription and protein expression levels of S1P, S2P, and RUNX2 in the sh-TGF-β group. OE S1P and OE S2P effectively counteracted the effect of sh-TGF-β on the protein and transcription levels of RUNX2 (Fig. 8C–E). Finally, immunofluorescence staining of the different transfection groups was performed using GhostPepper peptide/RUNX2. According to the staining results, the sh-TGF-β group showed a significant decrease in the level of expression of the RUNX2 protein compared to the sh-TGF-β-NC group ($P < 0.05$), while the sh-TGF-β + OE S1P and sh-TGF-β + OE S2P groups exhibited a significant increase in the level of expression of the RUNX2 protein compared to the sh-TGF-β group ($P < 0.05$) (Fig. 8F). The results of supplementary experiments indicated that TGF-β regulates the expression of S1P and S2P, forming a feedback loop with ATF6/-N to participate in the regulation of SEC24D-mediated cell osteogenesis (Supplementary Material 1).

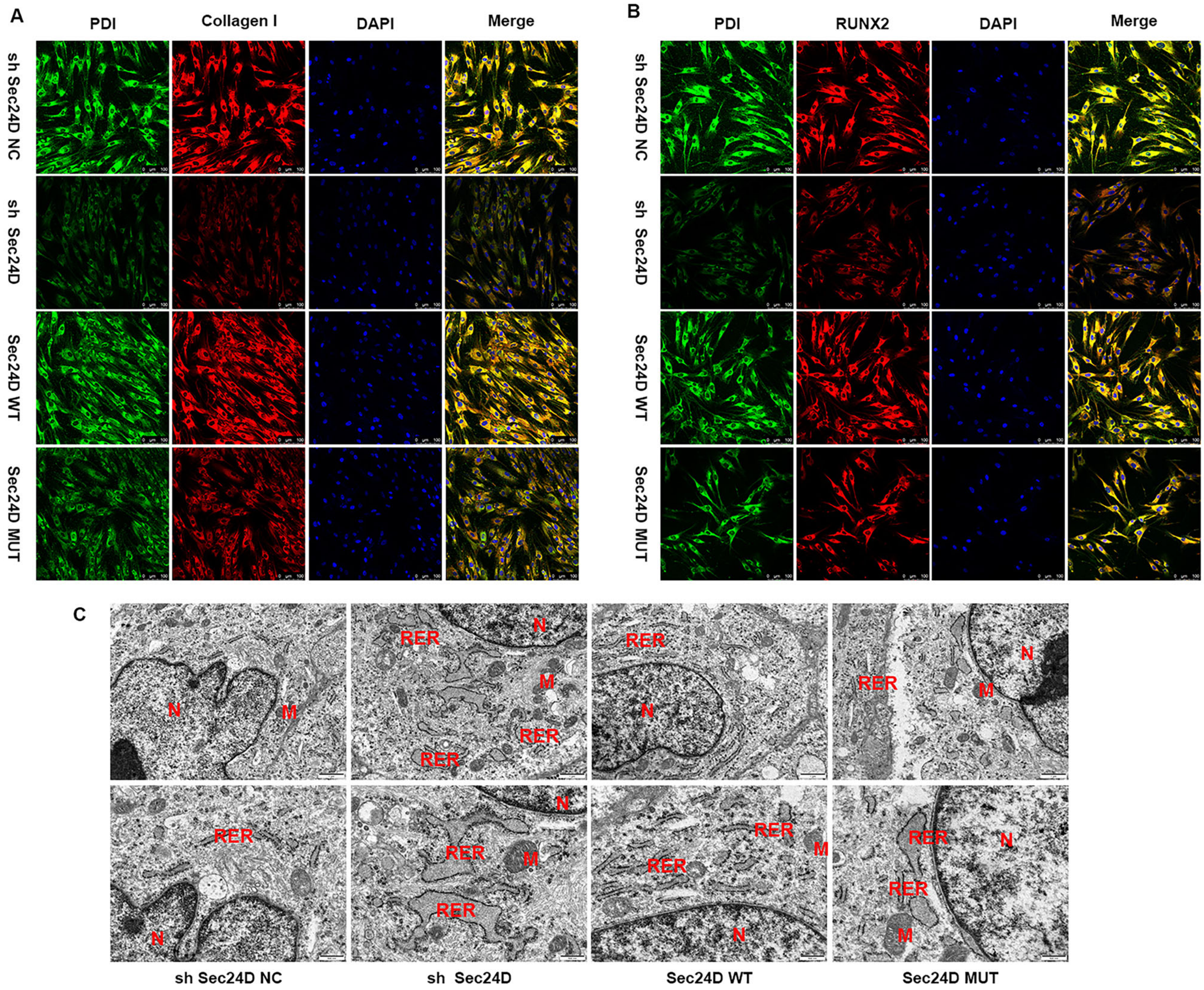

Fig. 4 | The SEC24D mutation downregulates RUNX2 and promotes ER stress. **A** Immunofluorescence staining of different transfection groups for protein disulfide isomerase (PDI)/Colla1. **B** Immunofluorescence staining of different transfection groups for protein disulfide isomerase (PDI)/RUNX2. **C** Transmission electron microscopy observation of different transfection groups. In the sh SEC24D-NC group, a track-like dense and coherent arrangement with ribosomes attached to the ER surface was observed. In the sh-SEC24D group, swelling, fragmentation, and disrupted coherence with detached ribosomes were observed. A lower ER status was detected in the SEC24D-MUT group than in the SEC24D-WT group.

TGF-β signaling pathway participates in SEC24D-regulated osteogenic differentiation of RUNX2. To confirm the involvement of the TGF-β signaling pathway in the SEC24D-mediated regulation of osteogenesis, experiments were performed using the sh-SEC24D-NC, sh-SEC24D, and sh-SEC24D/KRFK TFA groups. Cells from different groups underwent ALP staining. Compared to the sh-SEC24D-NC group, the sh-SEC24D group showed a significant decrease in the ALP content ($P < 0.05$), while the sh-SEC24D/KRFK TFA group exhibited a significant increase in ALP content compared to the sh-SEC24D group ($P < 0.05$) (Fig. 9A). Subsequently, Safranin O staining was performed to validate the results. Compared to the sh-SEC24D-NC group, the sh-SEC24D group showed a significant decrease in Safranin O content ($P < 0.05$), whereas, the sh-SEC24D/KRFK TFA group showed a significant increase in Safranin O content compared to the sh-SEC24D group ($P < 0.05$) (Fig. 9B). The results of the qPCR and WB analyses revealed that KRFK TFA effectively regulated the protein and transcription levels of RUNX2 (Fig. 9C–E). Immunofluorescence staining revealed a significant decrease in the level of expression of the RUNX2 protein in the sh-SEC24D group compared to that in the sh-SEC24D-NC group ($P < 0.05$), while the sh-SEC24D/KRFK TFA group exhibited a significant increase in the level of expression of the RUNX2 protein compared to the SEC24D group ($P < 0.05$) (Fig. 9F).

Discussion

In 1987, Cole and Carpenter described a new variant of OI, which is known as Cole Carpenter syndrome[20]. Along with severe bone fragility, the main features of this syndrome are craniosynostosis, communicating hydrocephalus, ocular proptosis, marked postnatal growth failure, and distinctive facial appearance[21]. Two subtypes of the syndrome have been identified, including CLCRP1, which is autosomal dominant and caused by *P4HB* gene mutation[22], and CLCRP2, which is autosomal recessive and caused by *SEC24D* gene mutation[10]. Only five other studies of CLCRP2 have been reported, and less than a dozen variants in *SEC24D* have been detected, which greatly limits the understanding of this disease (Table 1)[10,12–14].

In this study, we recruited a patient who suffered multiple fractures, and her physical features and bone histopathological findings indicated OI conditions. In subsequent genetic testing by WES, we identified the causative compound heterozygous variation of this gene. Additionally, we performed several in-depth in silico analyses of the effect of one of these variants, p.R313H, on the intermolecular structure of the protein, which may provide insights into rapidly investigating the effects of gene mutations.

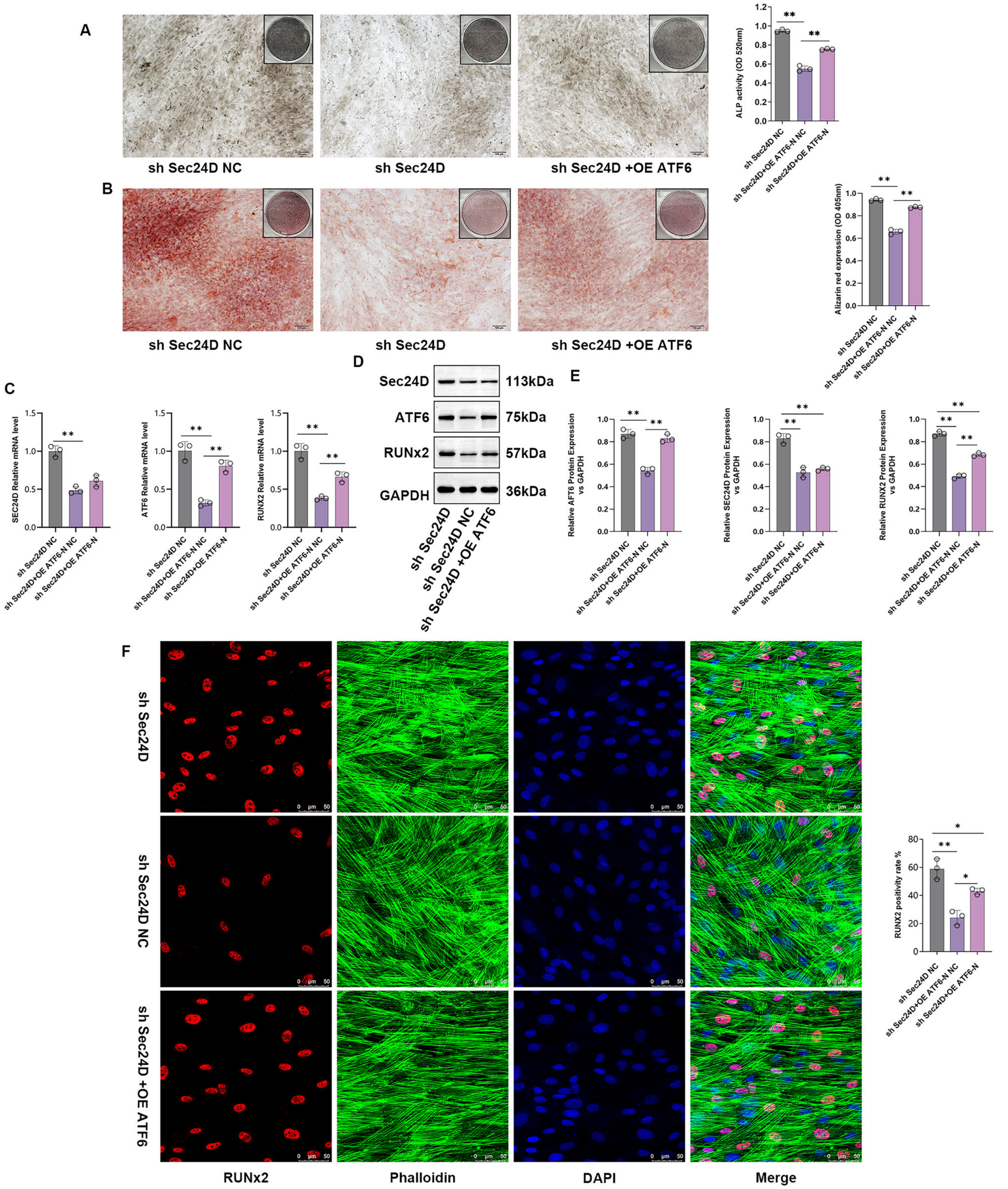

Fig. 5 | SEC24D Regulates Osteogenesis by Modulating the Expression of RUNX2 and ATF6-N. A ALP staining and quantification in different transfection groups. **B** Alizarin Red staining and quantification in different transfection groups. **C** Relative expression levels of *SEC24D*, *ATF6-N*, and *RUNX2* mRNA in different transfection groups. **D** Protein expression levels of SEC24D, ATF6-N, and RUNX2 in different transfection groups. **E** Western blot (WB) statistical analysis. **F** Immunofluorescence staining and quantification of Ghostine/RUNX2 in different transfection groups. n = 3 independent experiments. The error bars are equivalent throughout the Figure.

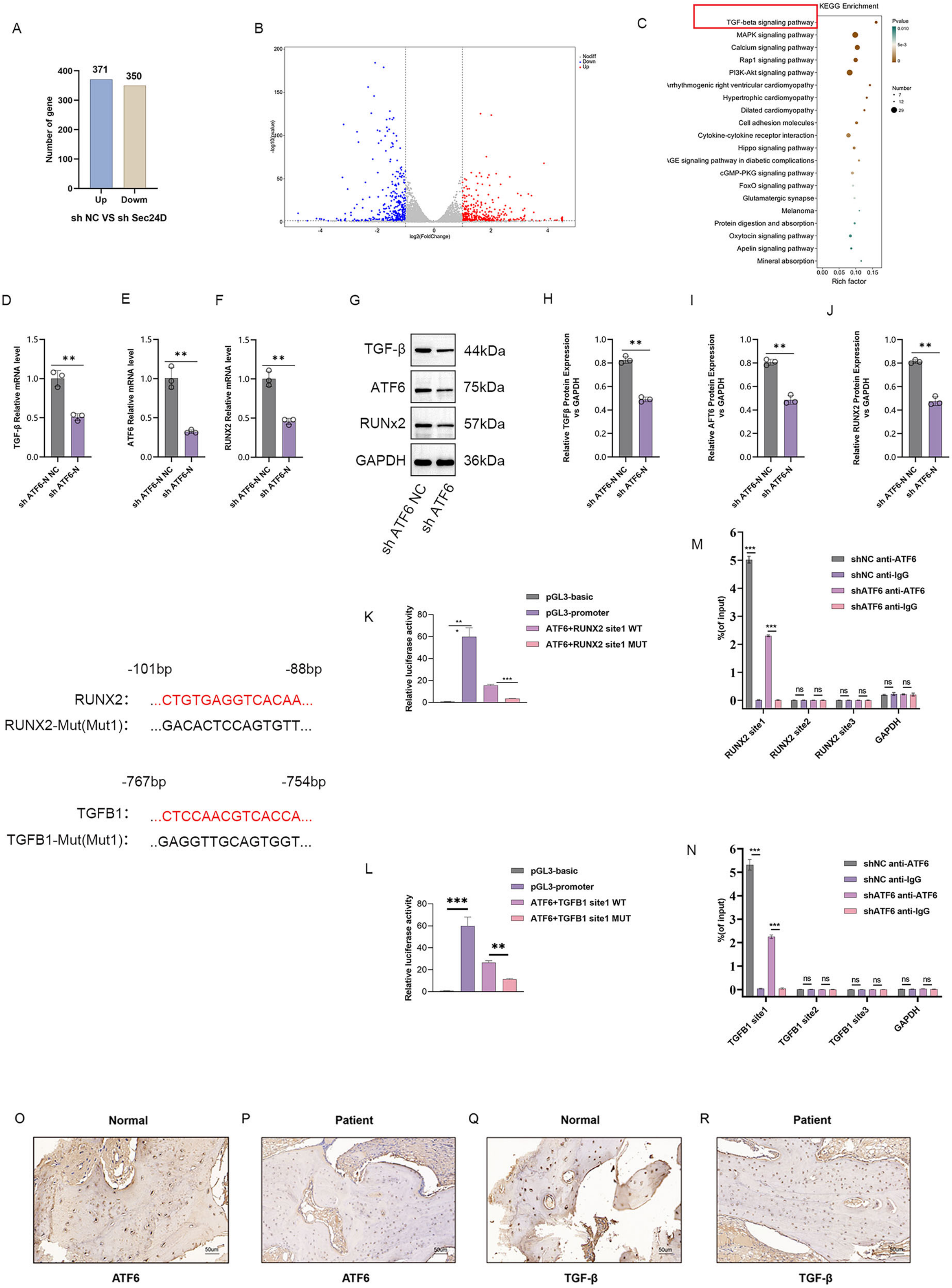

Fig. 6 | Transcriptomic Sequencing to Observe the Potential Effect of SEC24D Knockdown on Osteogenic Differentiation, revealing that ATF6-N regulates the Transcription of RUNX2 and TGF-β. A Venn diagrams. **B** Heatmaps. **C** KEGG analysis. **D**, **E**, **F** Expression levels of *ATF6-N*, *TGF-β*, and *RUNX2* mRNA in different transfection groups. **G**–**J** WB statistical analysis and relative protein expression levels of ATF6-N, TGF-β, and RUNX2 in different transfection groups. **K**, **L** Luciferase reporter assay, and **M**-**N** ChIP Experiment demonstrate that ATF-N can act on the transcription of Runx2 and TGFβ, respectively. **O**–**R** Immunohistochemistry detection of ATF6 and TGF-β protein expression levels in bone tissues of patients and normal people. $n = 3$ independent experiments. The error bars are equivalent throughout the Figure.

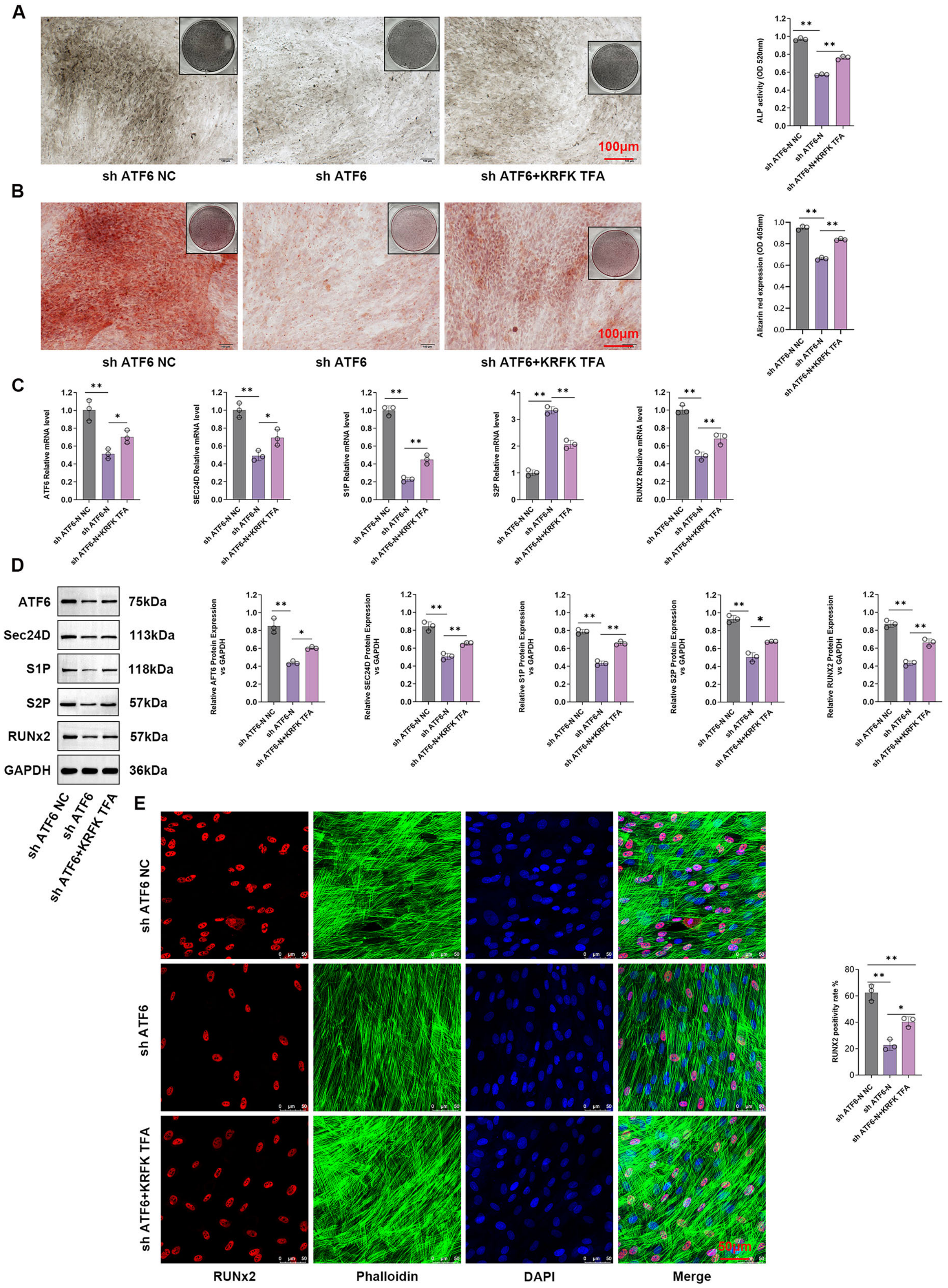

Fig. 7 | Involvement of the TGF-β signaling pathway in the SEC24D-regulated osteogenic differentiation of RUNX2 cells. **A** ALP staining and statistics of different transfection groups. **B** Alizarin red staining and statistical analysis of the different transfection groups. **C** Relative expression levels of *SEC24D*, *ATF6-N*, and *RUNX 2* mRNA in different transfection groups. **D** Differently transfected histone expression levels and WB statistical analysis. **E** Immunofluorescence staining and statistics of the ghost pen cyclic peptide/RUNX2 ratio in different transfection groups. *n* = 3 independent experiments. The error bars are equivalent throughout the Figure.

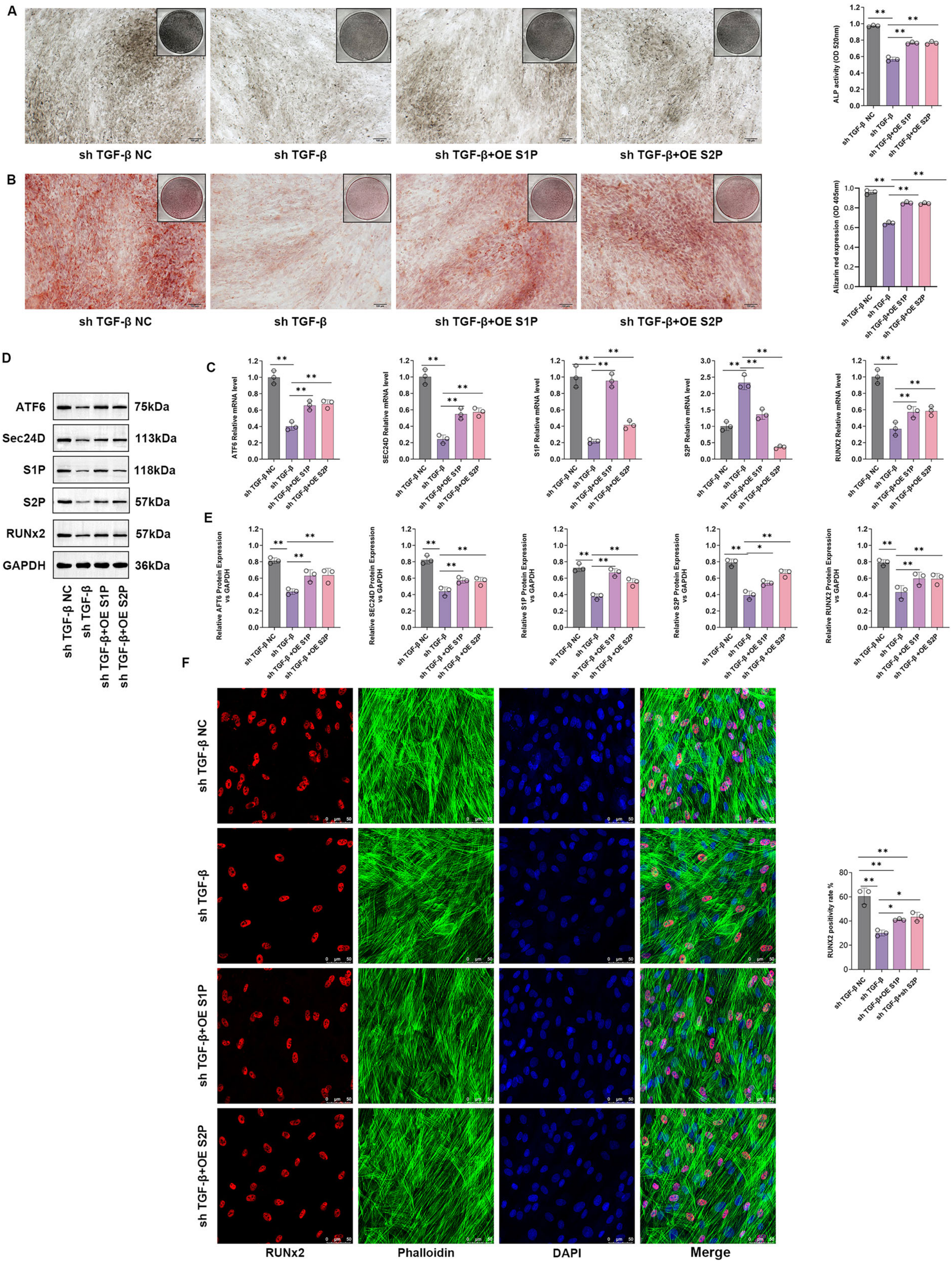

Fig. 8 | TGF-β regulates the expression of S1P and S2P. A ALP staining and quantification in different transfectio n groups. **B** Safranin O staining and quantification in different transfection groups. **C** Relative expression levels of *S1P*, *S2P*, *ATF6*, *SEC24D*, and *RUNX2* mRNA in different transfection groups. **D** Relative protein expression levels of S1P, S2P, ATF6, SEC24D, and RUNX2 in different transfection groups. **E** WB statistical analysis. **F** Immunofluorescence staining of different transfection groups using GhostPepper peptide/RUNX2. *n* = 3 independent experiments. The error bars are equivalent throughout the Figure.

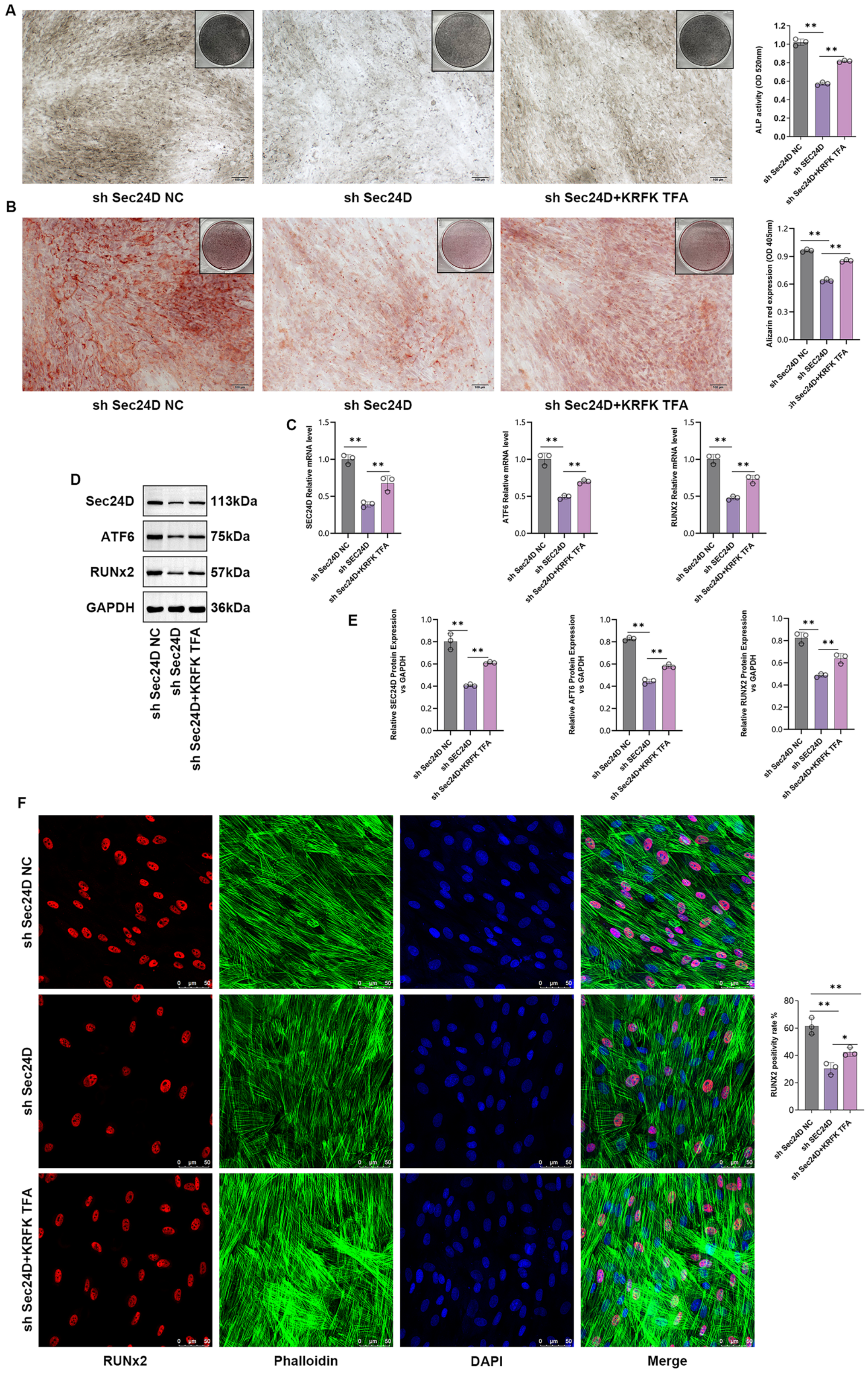

Fig. 9 | The involvement of the TGF-β signaling pathway in the regulation of RUNX2 osteogenic differentiation mediated by SEC24D. **A** ALP staining and statistical analysis of different transfection groups. **B** Alizarin Red staining and statistical analysis of different transfection groups. **C** Relative expression levels of *SEC24D*, *ATF6*, and *RUNX2* mRNA in different transfection groups. **D** Protein expression levels of SEC24D, ATF6, and RUNX2 in different transfection groups. **E** Western blot (WB) analysis. **F** Immunofluorescence staining and statistical analysis of different groups transfected with Ghost Pepper/RUNX2. *n* = 3 independent experiments. The error bars are equivalent throughout the Figure[37].

Table 1 | Osteogenesis imperfecta associated variations in *SEC24D* gene reported in literature and in this study (cited from HGMD*; Transcript No.: NM_014822.4; Protein No.: NP_055637.2)

No.	Genomic position [hg 19]	Genomic alteration	Protein alteration	Pathogenicity class* (HGMD)	Rank Score (HGMD)	dbSNP* No.	Reference (PMID*)
1	Chr4: 119,644,725	c.3044 C > T	p.S1015F	DM	0.70	rs760670617	25683121
2	Chr4: 119,649,741	c.2933 A > C	p.Q978P	DM	0.82	rs786204846	25683121
3	Chr4: 119,652,497	c.2842 T > C	p.S948P	DM	0.95	rs1175597762	27942778
4	Chr4: 119,652,616	c.2723 G > A	p.C908Y	DM	0.29	rs1182434832	27942778
5	Chr4: 119,659,416	c.2496 G > T	p.Q832H	DM	0.35	/	26467156
6	Chr4: 119,674,015	c.1450 C > T	p.R484*	DM	0.99	rs1372766642	30462379
7	Chr4: 119,718,941	c.938 G > A	p.R313H	DM	0.99	rs148676365	27942778; This study
8	Chr4: 119,727,036	c.875 C > T	p.P292L	DM	0.77	/	27942778
9	Chr4: 119,736,666	c.613 C > T	p.Q205*	DM	0.99	rs786204845	25683121
10	Chr4: 119754738	c.113dupC	p.Thr39Asnfs*16	DM	/	rs759594785	26467156
11	Chr4:119653953-119653955	c.2609_2610delGA	p.R870fs*10	/	/	/	This study

*HGMD: http://www.hgmd.cf.ac.uk/ac/index.php.
DM: Disease causing mutation.
dbSNP database: https://www.ncbi.nlm.nih.gov/snp/.
PMID: PubMed ID (https://pubmed.ncbi.nlm.nih.gov/).

Besides playing a role in skeletal dysplasia, *SEC24D* was also found to be associated with other disorders, such as autism spectrum disorders[23], intellectual disability[24], Brittle Cornea Syndrome[25], and rheumatoid arthritis[26]. However, these inconsistent reports lack support, and there is no strong functional experimental evidence.

The structural and functional basis of cargo membrane protein discrimination by the human COPII coat machinery was elucidated more than 15 years ago[11,27]. However, the mechanism by which specific COPII components influence specific tissue or organ development needs to be determined. As an important COPII component, SEC24D was found in fish models to affect vertebral and bone morphogenesis through extracellular matrix protein transport and cause craniofacial defects[28–30]. The combined loss of SEC24C and SEC24D results in neural crest migration and condensation deficits, indicating that SEC24D activity is essential for chondrocyte maturation; however, SEC24C and SEC24D compensate for each other in the early stages of cartilage development[31,32]. Early embryonic lethality was observed in mice severely deficient in SEC24D, while a hypomorphic SEC24D allele permitted survival to mid-embryogenesis[33]. However, few in vitro and in vivo studies have investigated the mechanism by which SEC24D affects bone formation in humans, which limits our understanding of CLCRP2[34,35].

In this study, we conducted a series of experiments to investigate the mechanism by which SEC24D regulates the osteogenic differentiation of hBMSCs. First, hBMSCs were subjected to SEC24D knockdown or mutation (with the p.R313H overexpression vector), and several osteogenic markers were detected by WB after transfection. Then, the osteogenic differentiation ability of hBMSCs was recorded and evaluated by ALP staining and Alizarin red staining. The results showed that SEC24D under expression downregulated the expression of multiple osteogenic markers and significantly decreased the osteogenic differentiation potential of hBMSCs. The effect of mutations was similar but weaker. Immunofluorescence experiments confirmed that RUNX2 and Collagen I, two important osteogenic molecules, were significantly affected by low SEC24D expression; interestingly, PDI was also affected, suggesting that it might influence ER stress and UPR, which is also important for the preservation of osteogenic potential[36]. The TEM results also indicated that low SEC24D expression disrupted the morphology and function of the ER.

The activation of UPR and IRE1α signaling is associated with SEC24D upregulation[37]. In Neuro-2a cells, ER stress and UPR can increase SEC24D expression[38]. These findings highlighted the correlation between UPR and SEC24D. Therefore, in subsequent experiments, we first analyzed UPR-associated proteins (ATF6, IRE1α, and PERK)[39,40] and the proteins involved in the folding pathway (ATF4, CHOP, GADD34, HERP, BIP, and SXBP1)[41–44] using transcriptome sequencing data from SEC24D-knockdown cells. Additionally, combined with the in silico interaction analysis, we targeted the molecule ATF6. During ER stress, ATF6 enters the Golgi via COPII transport and is sequentially hydrolyzed by the proteases S1P and S2P in the Golgi, releasing the soluble transcription factor ATF6-N, which enters the nucleus to play a role in transcription and relieve ER stress[45,46]. ATF6 plays an important role in bone development and can stimulate osteogenic differentiation by upregulating osteocalcin and RUNX2 transcription[47–50]. Won Gu et al. found that BMP2 regulates osteocalcin gene expression through the ATF6 pathway activated by ER stress, thus stimulating osteoblast differentiation[50]. A study also showed that an increase in SEC24D expression at condensed ER exit sites was associated with the attenuated translocation of ATF6 to the nucleus in Neuro-2a cells[38]. Our results showed that ATF6 expression decreased after SEC24D knockdown and ATF6 overexpression reversed the effect of SEC24D knockdown on the osteogenic differentiation of hBMSCs to a certain extent. Similarly, ATF6-N has a similar effect. We speculated that ATF6 is involved in the regulatory effect of SEC24D on osteogenic differentiation, but the underlying mechanism needs to be elucidated.

We also performed a KEGG (Kyoto Encyclopedia of Genes and Genomes) clustering analysis of the above transcriptome data and found that the TGF-β pathway was significantly suppressed after SEC24D was knocked down. TGF-β, the most abundant signaling molecule in the bone matrix, is essential for osteoblast differentiation and bone formation[51,52]. It also plays an important role in regulating the functions of mesenchymal stem cells (MSCs) in bone metabolism. The interruption of TGF-β signaling in bone metabolism forms the basis for congenital defects, acquired diseases, and bone tissue healing defects[53]. However, views on the role of TGF-β signaling in MSC osteogenic differentiation in some in vitro and in vivo studies are conflicting. The absence of TGF-β receptor 1 (TR1) in primary neonatal calvarial cells of mice inhibits osteogenic differentiation[54]. Additionally, TGF-β treatment was found to inhibit the osteogenic differentiation of mesenchymal progenitor cells (MPCs), and high levels of TGF-β1 in periodontitis were found to decrease the osteogenic differentiation of MSCs[55]. When ATF6-N was knocked down, TGF-β was also inhibited, and RUNX2 expression was downregulated. Thereafter, we confirmed that ATF6-N can positively regulate the transcription of TGF-β and RUNX2 via bioinformatics analysis and luciferase assays. We then used KRFK TFA, a polypeptide activator of TGF-β, to perform a recovery experiment. The results showed that external activation of TGF-β could partly prevent the effects of knocking down ATF6-N, including the inhibition of osteogenic differentiation in hBMSCs and the downregulation of the expression of osteogenic markers. The external activation of TGF-β also upregulated the expression of S1P and S2P, which led us to speculate that TGF-β can also react to the hydrolysis and activation of ATF6. Subsequent comprehensive experimental results confirmed this hypothesis, i.e., TGF-β can positively regulate the expression of S1P and S2P, form a feedback loop mechanism with ATF6, and jointly regulate osteogenic differentiation of hBMSCs (Fig. 8 and S2). Knocking down TGF-β unexpectedly also decreased the mRNA level of *ATF6*, suggesting that another larger regulatory network might be present that needs to be further characterized. Finally, we treated SEC24D-knockdown cells with KRFK TFA and recovered its destructive effect on osteogenic differentiation, which provides some clues for the treatment of the corresponding disease CLCRP2.

Overall, in this study, we conducted comprehensive clinical, imaging, pathological, and genetic analyses on a patient with OI. The findings showed that the patient had CLCRP2 disease caused by the *SEC24D* biallelic mutation. In subsequent experiments, we demonstrated that the depletion of SEC24D was associated with the regulation of osteogenic differentiation in hBMSCs through the ATF6/TGF-β/RUNX2 regulatory loop, and this mechanism of action provides an important basis for the development of targeted therapeutics.

Methods

This study was prospectively reviewed and approved by the Ethics Committee of the Shijiazhuang Obstetrics and Gynecology Hospital (approval no. 20240057), and all participants provided signed informed consent. All procedures performed in studies involving human participants followed the Declaration of Helsinki 1964 and its later amendments or comparable ethical standards.

Participants

A three-year-old female patient was initially referred to our department due to damage to the right thigh after an accidental fall in December 2014. We performed routine diagnosis and three surgical procedures for multiple fractures within six years, along with pathological biopsy of bone tissue during one surgery. We advised her family to undergo genetic testing in 2020 to identify the potential cause.

Hematoxylin and eosin (H&E) and immunohistochemistry (IHC) staining

During one surgery, the femoral tissues were extracted, fixed in 4% paraformaldehyde solution, and embedded in paraffin, and then, thin sections (4 μm thick) were cut. Immunohistochemical staining and H&E staining were performed on tissue sections. Immunohistochemical staining analysis was performed as described in another study[56]. Before antigen retrieval, the tissue sections were dewaxed and immersed in water. After treatment with H_2O_2, the tissue sections were blocked in 5% goat serum for 30 min. The sections were then incubated overnight at 4 °C with anti-RUNX2 (1:400, Abcam) and anti-OCN (1:400, Abcam) antibodies. The following day, the slides were incubated with anti-rabbit IgG (1:500, Abcam) and visualized using DAB (Invitrogen, USA).

Genetic detection

Genomic DNA was extracted from peripheral blood samples collected from the patient and her parents using a QIAamp DNA Blood Mini Kit (Qiagen, Germany). Chromosomal microarray analysis (CMA) was performed using the Affymetrix CytoScan 750 K platform, following the manufacturer's instructions (Affymetrix, USA).

Trio-whole-exome sequencing was performed to detect the sequence variants in the sample from the proband, as described in our previous study[57]. Briefly, the target-region sequences were enriched using the Agilent Sure Select Human Exon Sequence Capture Kit, V5 + UTR (Agilent, USA). DNA libraries were screened by quantitative PCR assays, and the size, distribution, and concentration of these libraries were determined using an Agilent Bioanalyzer 2100 (Agilent, USA). The NovaSeq 6000 platform (Illumina, Inc.) and ~150 bp paired-end reads were used to sequence the DNA (~ 300 pM per sample) using the NovaSeq Reagent Kit. The sequencing raw reads (quality level Q30% > 90%) were aligned to the human reference genome (accession no: hg19/GRCh37) via the Burrows-Wheeler Aligner tool, and PCR duplicates were removed using Picard v1.57. Variant calling was performed using the Verita Trekker® Variants Detection system (v2.0; Berry Genomics, China) and the Genome Analysis Tool Kit (https://software.broadinstitute.org/gatk/). Next, the annotation tools ANNOVAR v2.0[58] and Enliven® Variants Annotation Interpretation systems (Berry Genomics) were used to provide information to establish the criteria of the common guidelines provided by the American College of Medical Genetics and Genomics (ACMG)[59]. To interpret pathogenicity, three frequency databases (1000G_2015aug_eas, https://www.internationalgenome.org; ExAC_EAS, http://exac.broadinstitute.org; gnomAD_exome_EAS, http://gnomad.broadinstitute.org) and HGMD pro v2019 (Human Gene Mutation Database) were used. The Revel score (for pathogenicity prediction)[60] and the pLI score (representing the tolerance for truncating variants) were also used.

As a confirmatory method, Sanger sequencing was performed using a 3500DX Genetic Analyzer (Applied Biosystems, USA).

In silico structural and molecular dynamics analysis

The evolutionary conservation of the amino acid (AA) residue affected by the identified missense variant was analyzed using MEGA7 (http://www.megasoftware.net/previousVersions.php) with default parameters.

The SWISS-MODEL program was used for modeling the LRP6 PE3/4 domains containing the mutation site using the crystal structure PDB:3S2K (http://www1.rcsb.org/) with an X-resolution of 2.8 Å as the template[61]. Molecular dynamics (MD) prediction analysis was performed with GROMACS (version 2020.6)[62]. The detailed methods and corresponding results are included in Supplementary Material 1.

Cell culture

To elucidate how the depletion of SEC24D affects the osteogenic differentiation of stem cells, we conducted several in vitro experiments. The hBMSCs (CP-H166, Procell Life Science & Technology Co., Ltd.) were routinely revived and placed in a pre-prepared complete medium. The cells were cultured at 37 °C in a CO_2 incubator with 5% humidity. Cell passages were performed using 0.25% trypsin digestion.

Cell transfection

In order to knock out SEC24D or ATF6 in vitro, SEC24D-shRNA or ATF6-shRNA was transfected into cells using Lipofectamine 2000 (Invitrogen, Carlsbad, CA, USA) according to the manufacturer's instructions. In order to overexpress ATF6, cells were transfected with recombinant adenovirus (AdV5/F35, vigene Biosciences, Jinan, Shandong, China). The titer for usage is 1×10E10-11 vp/ml. The hBMSCs in the log phase were seeded in six-well cell culture plates. When the cell density reached about 70%, the adenovirus solution was added to the different groups. The NC group (hBMSCs cultured normally) was also included, with six parallel samples in each group. Subsequent experimental procedures were conducted after 48 h.

CCK-8 Assay

Cells were seeded at a density of 1.0×10^3 cells/well in a 96-well plate and cultured at 37 °C with 5% CO_2 for 24 h. After 24 h of serum starvation, five replicate wells were set. After treatment for 48 h, the original culture medium was discarded, and a mixture of CCK-8 reagent and medium was added to each well in a 1:9 ratio. The absorbance was measured at 450 nm using a microplate reader, and cell viability (%) was calculated as [(experimental group-blank group)/(control group-blank group)]×100%.

ELISA

Cells digested with 0.25% trypsin were cultured and treated with MLN4924 for 4 h after routine cultivation. The specific procedures were performed following the instructions of the ELISA kit. The absorbance was measured at 450 nm using a microplate reader to determine the OD.

ALP staining

The hBMSCs from each group were washed twice with phosphate-buffered saline (PBS) after seven days of culture. After fixation with ethanol for 1 h at 4 °C, ALP staining solution was added, and after 30 min of incubation in the dark, the cells were observed. ALP activity was determined following the instructions provided with the ALP activity assay kit.

Alizarin red s staining

The hBMSCs from each group were transfected for 6 h, and the medium was changed simultaneously with the addition of 50 mg/L vitamin C and 10 mmol/L β-glycerophosphate. After cultivation for 14 days, the culture medium was discarded, and the cells were fixed with 0.05% glutaraldehyde at 4 °C for 10 min. After washing thrice with deionized water (ddH$_2$O), the sections were stained with 0.4% Alizarin Red S for 5 min. After staining and washing with ddH$_2$O, the cells were observed under a microscope. For further quantitative analysis of calcified nodules, after capturing images under a microscope, cells from all groups were washed twice with PBS. Then, 10% cetylpyridinium chloride (prepared in 10 mmol/L pH 7.0 phosphate buffer) was added, and the absorbance (A) was measured at 570 nm using a microplate reader.

Transcriptome analysis

Total RNA was extracted from the cells with TRIzol (Invitrogen). RNA integrity was assessed using the RNA Nano 6000 Assay Kit of the Bioanalyzer 2100 system (Agilent). All the samples had integrity numbers greater than 7.0. Libraries were prepared using a NEBNext Ultra RNA Library Prep Kit (Illumina). The products were purified (AMPure XP system), and the library quality was assessed on an Agilent Bioanalyzer 2100 system. Next, the libraries were pooled and sequenced for 150 bp paired-end reads on a NovaSeq 6000 sequencing system (Illumina). The RNA-seq data were converted to FASTQ format, filtered, and used to perform Q20, Q30, and GC calculations. The paired-end clean reads were aligned to the reference genome using HISAT2 v2.0.5. Feature Counts v1.5.0-p3 was used to determine the number of reads mapped to each gene. Then, the fragments per kilobase of exon per million fragments mapped(FPKM)of each gene was calculated based on the length of the gene and the read count mapped to this gene. Differential expression analysis of two conditions/groups (two biological replicates per condition) was performed using the DESeq2 R package (1.20.0). Genes with an adjusted *P* value ≤ 0.05 and log 2 (fold change) ≥1.0 were considered differentially expressed genes (DEGs). The Cluster Profiler R package was used for GO and KEGG enrichment analyses.

Western blotting (WB) analysis

Total protein was extracted from the hBMSCs in all groups using a protein extraction kit, and the protein concentration was determined using the BCA method. The samples were stored at −80 °C. Western blotting analysis was performed to detect protein expression. Then, 50 ug of protein sample was subjected to SDS-PAGE, membrane transfer, blocking, and incubation with primary antibodies (ATF6, 1:2000, Proteintech; RUNX2, 1:500, Proteintech; SEC24D, 1:500, Proteintech; TGF-β, 1:1000, Proteintech; OCN, 1:2000, Abcam; Collage1, 1:1000, Abcam; Osterix, 1:1000, Abcam; Osteonectin, 1:500, Proteintech; ALP, 1:1000, Proteintech; OPN, 1:1000, Proteintech; BGLAP, 1:500, ABclonal, GAPDH, 1:5000, Proteintech) overnight at 4 °C. The following day, the samples were incubated with (Goat Anti-Rabbit IgG H&L, 1:5000, abcam, Rabbit Anti-Mouse IgG H&L (HRP), 1:5000, abcam) at 37 °C for 1 h. Then, imaging, exposure, photography, and analysis were performed. The ratio of the grayscale value of the target protein to the grayscale value of the internal reference GAPDH was used as the relative level of expression of the target protein.

Immunofluorescence

hBMSCs were seeded at a density of 3 × 10^4 cells/mL on cell culture slides. After 24 h of grouping, the cells were treated with 4% paraformaldehyde for 10 min, followed by blocking with 10% sheep serum for 1 h. The slides were then incubated overnight at 4 °C with a RUNX2 antibody (1:400, Abcam). The following day, the cells were incubated with anti-rabbit IgG (1:500) for 1 h, followed by staining with iFluorTM 488-labeled ghost peptide working solution for 60 min at room temperature in the dark. Following nuclear counterstaining with DAPI solution, the slides were mounted with a mounting medium and observed and photographed under a confocal microscope.

Transmission electron microscopy (TEM)

Transmission electron microscopy was performed to observe the morphology of the mitochondria. The hBMSCs were collected and immediately fixed in 2.5% glutaraldehyde, dehydrated with ethanol and acetone, embedded in resin, and cut into thin sections (approx. 60 nm thick). Images were acquired using a transmission electron microscope at 100 kV [Leica].

Quantitative fluorescence PCR (QF-PCR)

Cells were lysed using TRIzol RNA extraction reagent, and then, chloroform was added for RNA extraction. Next, RNA was precipitated with isopropanol, washed with 75% ethanol, and finally, dissolved in RNase-free water. A high-capacity cDNA reverse transcription kit was used to reverse transcribe RNA into cDNA. In an RNase-free eight-tube strip, 3 μL of cDNA, 6.2 μL of RNase-free water, 0.4 μL of forward primer, 0.4 μL of reverse primer, and 10 μL of 2× Universal SYBR Green Fast Quantitative PCR Mix (from ABclonal, China) were added. The eight-tube strip was placed in a PCR machine, the reaction time and temperature were set according to the manual, and the reaction was initiated. PCR was performed using an ABI7500 real-time PCR detection system (Carlsbad, California, USA). By comparing with internal reference genes, the relative quantification of each amplicon in the proband, their available parents or relatives, and unrelated controls were calculated. The relative level of each amplicon ($2^{-\Delta Ct}$) was determined by comparing the difference in fold changes (Δ Δ Ct) between the control group and the proband sample. The standard deviation indicating the normalization of reference genes, was calculated and is shown as an error bar. Gene mapper software was used to visualize the results.

Luciferase reporter assay

Luciferase reporter vectors were constructed for ATF6 WT and ATF6 MUT. The hBMSCs were seeded at a density of 2 × 10^4/cm^2 in a 24-well plate. After incubation for 24 h, the cells were cotransfected with fluorescent enzyme reporter vectors and RUNX2/TGF beta plasmids. Fluorescent enzyme activity was detected using a dual-luciferase reporter gene system after 48 h.

ChIP Experiment

We conducted ChIP experiments following the instructions of the ChIP assay kit, with three repetitions. The cells were cultured in culture dishes until they reached 80–90% confluence. Then, 20 mL of cell culture medium containing 1% formaldehyde was added. The cells were incubated at room temperature for 10 min, and crosslinking was terminated by adding glycine. The cells were placed on ice and washed with pre-chilled PBS containing protease inhibitors. The cells were then scraped and collected into centrifuge tubes, followed by centrifugation at 4 °C and 800 r/min for 3 min. The cell pellet was resuspended in SDS lysis buffer containing protease inhibitors and then divided into 400 μL aliquots (about 4 × 10^6 cells per tube) for storage. The power, disruption time, pause time, and number of cycles of the ultrasonic disruptor were adjusted. The cells were disrupted on ice to generate chromatin DNA fragments of 200–1,000 bp. The disrupted samples were centrifuged at 4 °C and 12,000 r/min for 10 min, and the DNA was purified and analyzed by 1.5% agarose gel electrophoresis to observe the shearing effect. For each 100 μL of the lysate, 900 μL of ChIP dilution buffer containing protease inhibitors and 60 μL of protein G agarose were added. The mixture was incubated at 4 °C with rotation for 60 min, followed by centrifugation at 5,000 r/min for 1 min to collect the protein G agarose beads. The supernatant was transferred to a new centrifuge tube, and 10 μL (1%) was used as the input control. The corresponding antibodies were added to the remaining supernatant, with 1 μg of RNA polymerase II antibody used as a positive control, 1 μg of mouse IgG antibody used as a negative control, and 2 μg of primary antibody used for the test samples. The mixture was incubated overnight at 4 °C under constant shaking. Then, 60 μL of protein G agarose was added, and the mixture was incubated at 4 °C under constant shaking for 60 min, and then centrifuged at 5000 r/min for 1 min to carefully remove the supernatant. Finally, the protein G/antibody/transcription factor/DNA complex was sequentially washed with low salt wash buffer, high salt wash buffer, LiCl wash buffer, and TE buffer. Then, 200 μL of elution buffer was added to the complex, which was gently mixed by tapping the tube wall and left at room temperature for 15 min. After centrifugation at 5000 r/min for 1 min, the supernatant was collected. NaCl (5 mol/L) was added, and the mixture was incubated at 65 °C in a water bath for 5 h to reverse the crosslinking and obtain free DNA. RNase A was added and incubated at 37 °C for 30 min, followed by incubation with 0.5 mol/L EDTA, 1 mol/L Tris-HCl (pH 6.5), and proteinase K and incubation at 45 °C for 60 min. The DNA was purified using a compatible centrifugal column purification kit. Finally, PCR identification was performed.

Statistics and Reproducibility

All experiment was repeated three times. All data were presented as the mean ± standard deviation (SD). All statistical analyses were performed using SPSS (v.21.0; IBM, Tokyo, Japan). The differences between the two groups were determined by Student's t-tests. Two-way analysis of variance was performed for multigroup comparisons. Post hoc analysis for significant differences was performed using the Newman-Keuls method. All differences were considered to be statistically significant at $p < 0.05$. All graphs were generated using the GraphPad Prism software (v.6.0; GraphPad Software, Inc., La Jolla, CA, United States).

Reporting summary

Further information on research design is available in the Nature Portfolio Reporting Summary linked to this article.

Data availability

The sequencing results that support the findings of this study are openly available in NCBI Sequence Read Archive (SRA), reference number PRJNA1250759. The raw transcriptome data during the study are openly available in in NCBI Sequence Read Archive (SRA), reference number PRJNA1255777, (https://www.ncbi.nlm.nih.gov/sra/PRJNA1255777). The newly generated plasmids during the study are openly available in Addgene, Addgene ID:238505(https://www.addgene.org/238505/). Numerical source data for all graphs in the manuscript can be found in supplementary data file. Uncropped and unedited blot/gel images were included as supplementary information. All other data are available from the corresponding author (or other sources, as applicable) on reasonable request.

Received: 9 October 2024; Accepted: 6 May 2025;

References

1. Verma, K., Verma, M., Chaphalkar, A. & Chakraborty, K. Recent advances in understanding the role of proteostasis. *Fac. Rev.* **10**, 72 (2021).
2. Bonifacino, J. S. & Lippincott-Schwartz, J. Coat proteins: shaping membrane transport. *Nat. Rev. Mol. Cell Biol.* **4**, 409–414 (2003).
3. Kreis, T. E. & Pepperkok, R. Coat proteins in intracellular membrane transport. *Curr. Opin. Cell Biol.* **6**, 533–537 (1994).
4. Dell'Angelica, E. C. & Bonifacino, J. S. Coatopathies: Genetic disorders of protein coats. *Annu Rev. Cell Dev. Biol.* **35**, 131–168 (2019).
5. Miller, E. A. & Schekman, R. COPII - a flexible vesicle formation system. *Curr. Opin. Cell Biol.* **25**, 420–427 (2013).
6. Zanetti, G. et al. The structure of the COPII transport-vesicle coat assembled on membranes. *ELIFE* **2**, e00951 (2013).
7. Hutchings, J., Stancheva, V., Miller, E. A. & Zanetti, G. Subtomogram averaging of COPII assemblies reveals how coat organization dictates membrane shape. *Nat. Commun.* **9**, 4154 (2018).
8. Boyadjiev, S. A. et al. Cranio-lenticulo-sutural dysplasia is caused by a SEC23A mutation leading to abnormal endoplasmic-reticulum-to-Golgi trafficking. *Nat. Genet.* **38**, 1192–1197 (2006).
9. Bianchi, P. et al. Congenital dyserythropoietic anemia type II (CDAII) is caused by mutations in the SEC23B gene. *Hum. Mutat.* **30**, 1292–1298 (2009).
10. Garbes, L. et al. Mutations in SEC24D, encoding a component of the COPII machinery, cause a syndromic form of osteogenesis imperfecta. *Am. J. Hum. Genet.* **96**, 432–439 (2015).
11. Wendeler, M. W., Paccaud, J. P. & Hauri, H. P. Role of Sec24 isoforms in selective export of membrane proteins from the endoplasmic reticulum. *EMBO Rep.* **8**, 258–264 (2007).
12. Moosa, S. et al. Mutations in SEC24D cause autosomal recessive osteogenesis imperfecta. *Clin. Genet.* **89**, 517–519 (2016).
13. Zhang, H. et al. Novel mutations in the SEC24D gene in Chinese families with autosomal recessive osteogenesis imperfecta. *Osteoporos. Int* **28**, 1473–1480 (2017).
14. Takeyari, S. et al. Japanese patient with Cole-carpenter syndrome with compound heterozygous variants of SEC24D. *A. J. Med. Genet. A* **176**, 2882–2886 (2018).
15. Li, S. et al. Genotypic and phenotypic analysis in Chinese cohort with autosomal recessive osteogenesis imperfecta. *Front Genet.* **11**, 984 (2020).
16. Chen, X., Shen, J. & Prywes, R. The luminal domain of ATF6 senses endoplasmic reticulum (ER) stress and causes translocation of ATF6 from the ER to the Golgi. *J. Biol. Chem.* **277**, 13045–13052 (2002).
17. Sharma, R. B., Snyder, J. T. & Alonso, L. C. Atf6α impacts cell number by influencing survival, death and proliferation. *Mol. Metab.* **27s**, S69–s80 (2019).
18. Briggs, M. D., Dennis, E. P., Dietmar, H. F. & Pirog, K. A. New developments in chondrocyte ER stress and related diseases. *F1000Research* **9**, https://doi.org/10.12688/f1000research.22275.1 (2020).
19. Choi, Y., Lee, E. G., Jeong, J. H. & Yoo, W. H. 4-Phenylbutyric acid, a potent endoplasmic reticulum stress inhibitor, attenuates the severity of collagen-induced arthritis in mice via inhibition of proliferation and inflammatory responses of synovial fibroblasts. *Kaohsiung J. Med. Sci.* **37**, 604–615 (2021).
20. Cole, D. E. C. & Thomas, O. Carpenter. Bone fragility, craniosynostosis, ocular proptosis, hydrocephalus, and distinctive facial features: A newly recognized type of osteogenesis imperfecta. *J. Pediatr.* **110**, 76–80 (1987).
21. Amor, D. J., Savarirayan, R., Schneider, A. S. & Bankier, A. New Case of Cole-Carpenter Syndrome. *Am. J. Med. Genet.* **92**, 273–277 (2000).
22. Rauch, F. et al. Cole-Carpenter syndrome is caused by a heterozygous missense mutation in P4HB. *Am. J. Hum. Genet* **96**, 425–431 (2015).
23. Iossifov, I. et al. The contribution of de novo coding mutations to autism spectrum disorder. *Nature* **515**, 216–221 (2014).
24. Alazami, A. M. et al. Accelerating novel candidate gene discovery in neurogenetic disorders via whole-exome sequencing of prescreened multiplex consanguineous families. *Cell Rep.* **10**, 148–161 (2015).
25. Micheal, S. et al. Identification ofMutations in the PRDM5 Gene in Brittle Cornea Syndrome. *CORNEA* **35** (2016).
26. Rauch, F., Bardai, G. & Rockman-Greenberg, C. ALPL mutations in adults with rheumatologic disorders and low serum alkaline phosphatase activity. *J. Bone Miner. Metab.* **37**, 893–899 (2019).

27. Mancias, J. D. & Goldberg, J. Structural basis of cargo membrane protein discrimination by the human COPII coat machinery. *EMBO J* **27**, 2918-2928.
28. Ohisa, S., Inohaya, K., Takano, Y. & Kudo, A. sec24d encoding a component of COPII is essential for vertebra formation, revealed by the analysis of the medaka mutant, vbi. *Dev. Biol.* **342**, 85–95 (2010).
29. Sarmah, S. et al. Sec24D-dependent transport of extracellular matrix proteins is required for zebrafish skeletal morphogenesis. *PLOS One* **5**, e10367 (2010).
30. Lu, C. L. et al. Collagen has a unique SEC24 preference for efficient export from the endoplasmic reticulum. *Traffic* **23**, 81–93 (2022).
31. Melville, D. B. et al. The feelgood mutation in zebrafish dysregulates COPII-dependent secretion of select extracellular matrix proteins in skeletal morphogenesis. *Dis. Model Mech.* **4**, 763–776 (2011).
32. Adams, E. J. et al. Murine SEC24D can substitute functionally for SEC24C during embryonic development. *Sci. Rep.* **11**, 21100 (2021).
33. Baines, A. C., Adams, E. J., Zhang, B. & Ginsburg, D. Disruption of the Sec24d gene results in early embryonic lethality in the mouse. *PLOS One* **8**, e61114 (2013).
34. Curtis, S. W. et al. Rare variant modifier analysis identifies variants in SEC24D associated with orofacial cleft subtypes. *Hum. Genet.* **142**, 1531–1541 (2023).
35. Zhu, H., Su, Y., Wang, J. & Wu, J. Y. The role of vesicle trafficking genes in osteoblast differentiation and function. *Sci. Rep.* **13**, 16079 (2023).
36. Li, F. et al. Melatonin activates mitochondrial unfolded protein response to preserve osteogenic potential of senescent BMSCs via upregulating PDI-6. *Biochimie* **209**, 44–51 (2023).
37. Aartsma-Rus, A., Van Deutekom, J. C., Fokkema, I. F., Van Ommen, G. J. & Den Dunnen, J. T. Entries in the Leiden Duchenne muscular dystrophy mutation database: an overview of mutation types and paradoxical cases that confirm the reading-frame rule. *Muscle Nerve* **34**, 135–144 (2006).
38. Srinivasan, R. et al. Pharmacological chaperoning of nicotinic acetylcholine receptors reduces the endoplasmic reticulum stress response. *Mol. Pharmacol.* **81**, 759–769 (2012).
39. Xue, M., Irshad, Z., Rabbani, N. & Thornalley, P. J. Increased cellular protein modification by methylglyoxal activates endoplasmic reticulum-based sensors of the unfolded protein response. *Redox Biol.* **69**, 103025 (2024).
40. Kovaleva, V. et al. MANF regulates neuronal survival and UPR through its ER-located receptor IRE1α. *Cell Rep.* **42**, 112066 (2023).
41. Márton, M. et al. A systems biological analysis of the ATF4-GADD34-CHOP regulatory triangle upon endoplasmic reticulum stress. *FEBS Open Bio* **12**, 2065–2082 (2022).
42. Shen, W. B. et al. Obesity impacts placental function through activation of p-IRE1a-XBP1s signaling. *Front. Cell Dev. Biol.* **11**, 1023327 (2023).
43. Kopp, M. C., Larburu, N., Durairaj, V., Adams, C. J. & Ali, M. M. U. UPR proteins IRE1 and PERK switch BiP from chaperone to ER stress sensor. *Nat. Struct. Mol. Biol.* **26**, 1053–1062 (2019).
44. Zhang, Z. et al. The unfolded protein response regulates hepatic autophagy by sXBP1-mediated activation of TFEB. *Autophagy* **17**, 1841–1855 (2021).
45. Sharma, R. B., Snyder, J. T. & Alonso, L. C. Atf6alpha impacts cell number by influencing survival, death and proliferation. *Mol. Metab.* **27S**, S69–S80 (2019).
46. Oka, O. B. et al. ERp18 regulates activation of ATF6alpha during unfolded protein response. *EMBO J.* **38**, e100990 (2019).
47. Ma, M. et al. Erratum: ATF6 aggravates angiogenesis-osteogenesis coupling during ankylosing spondylitis by mediating FGF2 expression in chondrocytes. *iScience* **27**, 108768 (2024).
48. Xiong, Z., Jiang, R., Zhang, P., Han, X. & Guo, F. J. Transmission of ER stress response by ATF6 promotes endochondral bone growth. *J. Orthop. Surg. Res.* **10**, 141 (2015).
49. Guo, F. et al. ATF6a, a Runx2-activable transcription factor, is a new regulator of chondrocyte hypertrophy. *J. cell Sci.* **129**, 717–728 (2016).
50. Jang, W. G. et al. BMP2 protein regulates osteocalcin expression via Runx2-mediated Atf6 gene transcription. *J. Biol. Chem.* **287**, 905–915 (2012).
51. Cai, G. et al. Piezo1-mediated M2 macrophage mechanotransduction enhances bone formation through secretion and activation of transforming growth factor-β1. *Cell Prolif.* **56**, e13440 (2023).
52. Zhang, X. F. et al. TGF-β1-triggered BMI1 and SMAD2 cooperatively regulate miR-191 to modulate bone formation. *Mol. Ther. Nucleic Acids* **35**, 102164 (2024).
53. Song, I. W. et al. Targeting TGF-β for treatment of osteogenesis imperfecta. *J. Clin. Investig.* **132**, https://doi.org/10.1172/jci152571 (2022).
54. Matsunobu, T. et al. Critical roles of the TGF-beta type I receptor ALK5 in perichondrial formation and function, cartilage integrity, and osteoblast differentiation during growth plate development. *Dev. Biol.* **332**, 325–338 (2009).
55. Li, J. et al. TGFβ-induced degradation of TRAF3 in mesenchymal progenitor cells causes age-related osteoporosis. *Nat. Commun.* **10**, 2795 (2019).
56. Ren, L. X. et al. A Novel ZNF304/miR-183-5p/FOXO4 pathway regulates cell proliferation in clear cell renal carcinoma. *Front. Oncol.* **11**, 710525 (2021).
57. Yang, K. et al. Genetic analysis in fetal skeletal dysplasias by trio whole-exome sequencing. *Biomed. Res. Int.* **2019**, 1–8 (2019).
58. Wang, K. & Hakonarson, L. M. H. ANNOVAR: Functional annotation of genetic variants from next-generation sequencing data. *Nucleic Acids Res.* **38**, e164 (2010).
59. Richards, S. et al. Standards and guidelines for the interpretation of sequence variants: a joint consensus recommendation of the American College of Medical Genetics and Genomics and the Association for Molecular Pathology. *Genet. Med.* **17**, 405–424 (2015).
60. Ioannidis, N. M. et al. REVEL: An Ensemble Method for Predicting the Pathogenicity of Rare Missense Variants. *Am J. Hum. Genet.* **99**, 877–885 (2016).
61. Mancias, J. D. & Goldberg, J. Structural basis of cargo membrane protein discrimination by the human COPII coat machinery. *EMBO J.* **27**, 2918–2928 (2008).
62. Rakhshani, H., Dehghanian, E. & Rahati, A. Enhanced GROMACS: toward a better numerical simulation framework. *J. Mol. Model* **25**, 355 (2019).

Acknowledgements

The authors acknowledge the enrolled family for their participation in this study, and the expertise of Dr. Yu-qing You from Beijing MyGenostics Technology Co., Ltd., and Dr. Jin-wu Liu from Beijing MDKN Technology Co., Ltd. This study was supported by the Hebei Natural Science Foundation Precision Medicine Joint Fund Cultivation Project (No. H2021206242); the National Key Research and Development Program of China (2023YFC2705600); the Capital Clinical Characteristic Diagnosis and Treatment Technology Research and translational Application Project (Z221100007422012); Beijing Obstetrics and Gynecology Hospital, Capital Medical University, Beijing Maternal and Child Health Care Hospital(FCYYJC202403); Medical scientific research project of Health Commission of Hebei Province (20231661); and the Beijing Hospitals Authority Youth Program (No. QML20211401).

Author contributions

Q.G. and Ch.Y. designed the whole study scheme. YzL recruited the case and performed the clinical evaluation. J.Z., K.Y. and Q.L. conducted the genetic detection and data analysis. Hy.H., Ys.Y, and D.I.S, performed the structural and MD analysis. J.Z., K.,Y., and Wq.C. conducted the

immunostaining study and the subsequent molecular study. J.Z., K.Y. and Wq.C. wrote the original version of this manuscript, and all co-authors have read it and approved the submission.

Competing interests

The authors declare no competing interests.

Ethics approval and consent to participate

This study was approved by the Ethics Committee of Shijiazhuang Obstetrics and Gynecology Hospital (approval No. 20240057), and written informed consent was obtained from all participants.

Additional information

Supplementary information The online version contains supplementary material available at https://doi.org/10.1038/s42003-025-08175-9.

Correspondence and requests for materials should be addressed to Cheng-hong Yin or Qing Guo.

Peer review information *Communications Biology* thanks the anonymous reviewers for their contribution to the peer review of this work. Primary Handling Editors: Martina Rauner and Joao Valente. A peer review file is available.

Reprints and permissions information is available at http://www.nature.com/reprints

Publisher's note Springer Nature remains neutral with regard to jurisdictional claims in published maps and institutional affiliations.

Open Access This article is licensed under a Creative Commons Attribution-NonCommercial-NoDerivatives 4.0 International License, which permits any non-commercial use, sharing, distribution and reproduction in any medium or format, as long as you give appropriate credit to the original author(s) and the source, provide a link to the Creative Commons licence, and indicate if you modified the licensed material. You do not have permission under this licence to share adapted material derived from this article or parts of it. The images or other third party material in this article are included in the article's Creative Commons licence, unless indicated otherwise in a credit line to the material. If material is not included in the article's Creative Commons licence and your intended use is not permitted by statutory regulation or exceeds the permitted use, you will need to obtain permission directly from the copyright holder. To view a copy of this licence, visit http://creativecommons.org/licenses/by-nc-nd/4.0/.

© The Author(s) 2025